






Article

Finite Element Validation of an Energy Attenuator for the Design of a Formula Student Car

José A. López-Campos ¹, Jacobo Baldonado ¹, Sofía Suárez ¹, Abraham Segade ¹,
Enrique Casarejos ¹ and José R. Fernández ^{2,*}

¹ Departamento de Ingeniería Mecánica, Máquinas y Motores Térmicos y Fluídos, Escola de Enxeñaría Industrial, Campus As Lagoas Marcosende s/n, 36310 Vigo, Spain;

joseangellopezcampos@uvigo.es (J.A.L.-C.); jacobogonzalez.baldonado@uvigo.es (J.B.); sofiasgarcia@hotmail.es (S.S.); asegade@uvigo.es (A.S.); e.casarejos@uvigo.es (E.C.)

² Departamento de Matemática Aplicada I, Universidade de Vigo, ETSI Telecomunicación, Campus As Lagoas Marcosende s/n, 36310 Vigo, Spain

* Correspondence: jose.fernandez@uvigo.es; Tel.: +34-986-818-746

Received: 20 February 2020; Accepted: 11 March 2020; Published: 14 March 2020



Abstract: Passive safety systems of cars include parts on the structure that, in the event of an impact, can absorb a large amount of the kinetic energy by deforming and crushing in a design-controlled way. One such energy absorber part, located in the front structure of a Formula Student car, was measured under impact in a test bench. The test is modeled within the Finite Element (FE) framework including the weld characteristics and weld failure description. The continuous welding feature is almost always disregarded in parts included in impact test models. In this work, the FE model is fully defined to reproduce the observed results. The test is used for the qualitative and quantitative validation of the crushing model. On the one hand, the acceleration against time curve is reproduced, and on the other hand, the plying shapes and welding failure observed in the test are also correctly described. Finally, a model that includes additional elements of the car structure is also simulated to verify that the energy absorption system is adequate according to the safety regulations.

Keywords: impact attenuator; welding; nonlinear FEM; buckling initiator

1. Introduction

In high speed vehicle impacts the role of the structure is of uttermost importance, in that it must absorb as much energy as possible. The structure includes elements with a well defined stiffness and is designed to deform under impact so that the kinetic energy is transformed into plastic deformation. A proper design allows for a controlled deceleration, limiting the maximum acceleration values, all of which help to guarantee the survival probability for the passengers.

Formula Student cars are created and managed by teams of engineering students all over the world, modifying and improving the cars year after year. The FS 2017–2018 rules [1] define design conditions for a list of car components, in particular concerning the Energy Absorption system. This system must include an Impact Attenuator and an Anti-Intrusion Plate. This study focuses on an Impact Attenuator structure designed for a racing car under the Formula Student (FS) regulations.

The FS rules require that the dynamic response of the Energy Absorption system should be such that, for a 300 kg car impacting into a rigid barrier at 7 m/s speed, the acceleration peak cannot exceed the value 40 g, and the acceleration mean value must be below 20 g. The absorbed energy must be of at least 7350 J and permanent deformation cannot exceed the value of 25 mm.

Some Energy Absorber systems for FS cars are studied in different works. There are single and multiple thin-wall cell designs [2]; aluminum honeycomb structures [3] and mixed aluminum

structures with a honeycomb core and a sheet cover [4,5]. Due to the weight limitations for the FS cars, there are proposals to include composites [6,7], and alternative materials [8]. This work considers the simplest case of an Impact Attenuator, built with aluminum sheets welded together.

Impact Attenuators are tested under different conditions: static conditions [3,7], dynamical tests [4,6], and also fully installed in a car [5]. In the case studied, the test was carried out in a drop-tower, where only the attenuator was present (without any of the tubes from the chassis). Since the regulation requires a relevant part of the chassis to be present, we first construct a model that is validated with the results from the test. Then, we complete that model with part of the chassis, now complying with the regulation standards, to check if the energy absorption requirements established in the regulation are fulfilled.

To construct a model able to accurately reproduce the real behavior of the material, the plastic behavior is considered. This is usually the case in the simulation of this type of structures [9]. The novelty presented in this work is the addition of weld characteristics and weld failure to the absorber model. The welding is continuous and it is studied considering it as a discrete connection between nodes. Detailed models are rather common for spot-welded parts due to its generalized use in the automotive industry.

However, continuous welding is almost always disregarded for parts evaluated with explicit simulation [9,10]. For the simulation of the plates in spot-welds, Cheng [11] compared the performance of shell elements with purely three-dimensional elements, finding that the stress field in two-dimensional (2D) models and three-dimensional (3D) models were quite similar, even in the prediction of through-thickness stress. For the simulation of the spot-weld, it is usually proposed a one-dimensional (1D) model [12–14]. Xiang [15] compared 16 spot-weld models (1D, 2D and 3D) and drew two main conclusions. On the one hand, 1D rigid-bar models were accurate enough once the spot-weld model represent the dimension of the real spot-welds. On the other hand, rigid-node spot weld models were suitable for crash analysis when there is no spot-weld failure due to its least modeling effort. Therefore, the simplest models can describe the results accurately enough.

Almost always authors deal with Finite Element (FE) models under static conditions [11,15–17] and with no spot-weld failure [16,17]. Only a few works deal with spot-weld failure including true separation between nodes: authors in [13] consider a single non-linear spring under static conditions; in [12] is proposed a single spring where a damage function is defined but validated only with low strain rate tests. Literature where spot-weld failure definition is included in impact test is scarce [18–20]. In this work, we deal with weld failure in impact tests including a continuum welding type.

The proposed approach is different from usual works on fatigue failure described according to elastic laws or even non-linear approximations, which are only valid for static analysis. The novelty of the model presented here is based on the discretization of a continuum welding and its application to an impact problem, where the qualitatively results of the weld failure are reproduced.

Concerning the welding process, FE models enable virtual examination of the welding process [21] where the thermal cycle causes residual stresses and structural distortion of the affected parts. A review of different FE methods applied to welding processes is done by Marques et al. in [22]. The goal of some of the methods is evaluating residual stresses in welded joints [23,24], or inherent deformations due to thermal effects [25,26].

The control of imperfections is a major concern in mechanical systems [27], and in the presented case of this work the control of residual deformations is crucial because these deformations strongly define the buckling onset of thin-walled structures [28,29]. The structure may include defaults made in purpose to trigger the proper folding pattern [30,31] and consequently the proper behavior of the simulation. In a previous work [28] some of the present authors discussed the influence of the position of a deformation trigger in the folding pattern, and also tested the influence of weakened welded regions on the acceleration profile. In this new work, an improved definition of the welding model is used, reaching more accurate results once compared to experimental results.

The paper is structured as follows. In Section 2, the mathematical problem is properly defined and its numerical resolution is briefly commented. Then, we study two different models. First, in Section 3, we evaluate the attenuator in isolation, in the conditions that an experimental test was carried. Second, the attenuator together with the front part of the chassis is simulated, in order to reproduce the conditions required by the regulation for this type of test. This is shown in Section 4. Finally, some conclusions are presented in Section 5.

2. Mathematical Model and Numerical Resolution

In this section we provide the mathematical description of the mechanical problem, as well as some important details about the numerical resolution using the finite element method. The three-dimensional geometry of the energy attenuator is obtained from the real test. It consists of a truncated pyramid with rectangular basis and inscribed within an envelope with a prescribed size (see Figure 1). The material model as well as the model used in the welded parts are described next. However, the boundary conditions are detailed, for each particular case, in the following sections.

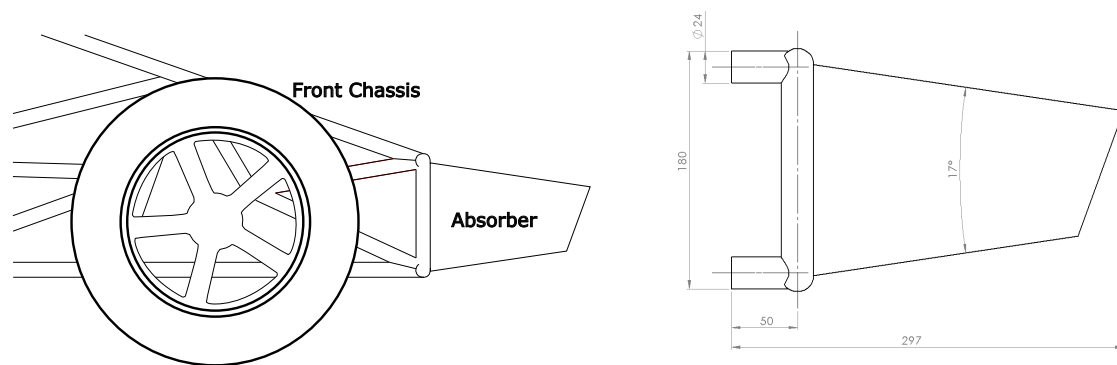


Figure 1. Left: Geometry of the impact attenuator (including part of the chassis). Right: Dimensions of the absorber (mm).

2.1. Plasticity

In order to define the material behavior for the attenuator, we used the classical definition of an elasto-plastic material with isotropic hardening. This avoids the Bauschinger effect when dealing with large deformations [32]. The material behaves as isotropic linear elastic until the yield condition is fulfilled. To define the yield condition the classical von Mises criterion is used (see [33] for details). This criterion is mainly based on the deviatoric stress tensor, so its definition is made according to the following equation:

$$f(J_2) = \sqrt{J_2} - \frac{\sqrt{3}}{3} \sigma_Y(\chi) = 0, \tag{1}$$

where J_2 represents the second invariant of the deviatoric stress tensor, and $\sigma_Y(\chi)$ states a dependence of the elastic yield stress on the constitutive parameters which defines the material hardening. In our case, we used the following expression:

$$\sigma_Y(\chi) = \sigma_{0Y} + E_t \varepsilon^p. \tag{2}$$

Here, σ_{0Y} , E_t and ε^p denote the constant elastic limit, the tangent modulus at time and the equivalent plastic strain (computed according to the von Mises criterion), respectively.

The deviatoric stress tensor is obtained through the decomposition of the full stress tensor into this deviatoric component p , and the volumetric one s :

$$\sigma = p \cdot \mathbf{I} + s. \tag{3}$$

Then, the second invariant is computed according to its definition:

$$J_2 = (\mathbf{s} : \mathbf{I})^2 + \mathbf{s} : \mathbf{s}. \tag{4}$$

Therefore, according to the previously detailed yield criterion, there are two possibilities for the $f(J_2)$ value. If $f(J_2) = 0$, the von Mises criterion is fulfilled, and therefore the material is yielding, while if $f(J_2) < 0$ the material behaves as linear elastic. In the case of $f(J_2) = 0$, the yielding behavior has to be governed, so a flow rule must be defined. It is generally written in terms of a plastic potential function. Since an incremental formulation is applied, we use the plastic potential to derive the plastic strain increment in the following form:

$$d\boldsymbol{\varepsilon}^p = d\lambda \cdot \nabla g, \tag{5}$$

where $d\lambda$ is a positive scalar of proportionality, $g(\boldsymbol{\sigma})$ is the plastic potential and the flow rule is governed by its gradient in terms of stress:

$$\nabla g_{ij} = \frac{\partial g}{\partial \sigma_{ij}}. \tag{6}$$

Considering that expression $g(\boldsymbol{\sigma}) = 0$ defines a surface in the stress domain, the flow rule equations suggest that yielding is produced in a normal direction to such surface. In addition, in this case we assume an associative flow rule, therefore the expression for $g(\boldsymbol{\sigma})$ is exactly the same as for $f(J_2)$. Finally, these definitions are used together with the constitutive relation to derive the stress increment as a function of strain increments:

$$d\boldsymbol{\sigma} = \mathbb{D} : d\boldsymbol{\varepsilon}^e = \mathbb{D} : (d\boldsymbol{\varepsilon} - d\boldsymbol{\varepsilon}^p) = \mathbb{D} : (d\boldsymbol{\varepsilon} - d\lambda \cdot \nabla f(J_2)). \tag{7}$$

2.2. Weld

To simulate the welding behavior, a discrete definition of the weld joint is used. We assume that the side plates that compose the attenuator are welded together. To perform such definition, the (conforming) nodes of adjacent parts are taken by pairs; each pair is perfectly joined using a rigid body with the geometry of a weld fillet and, in each computation cycle, the stress-state of such body is updated. If the stress fulfills the following criterion, the welding joint fails and the corresponding nodes are free to separate:

$$\sqrt{\sigma_n^2 + 3(\tau_n^2 + \tau_t^2)} \geq \sigma_f, \tag{8}$$

where σ_n is the normal stress, τ_n is the shear stress through the local direction OY , τ_t is the shear stress through the local direction OX and σ_f is a given parameter related to the welding strength. To evaluate such criterion, a local coordinate system has to be defined. To illustrate how the nodes of two different parts are connected and how the local coordinate system is defined, an example is shown in Figure 2.

The same definitions and procedures are applied to each pair of nodes that are welded together. Therefore, the continuous weld filled in the actual attenuator is approximated as a finite number of node's pairs joined with a breakable joint that is supposed to be able to reproduce the real weld behavior.

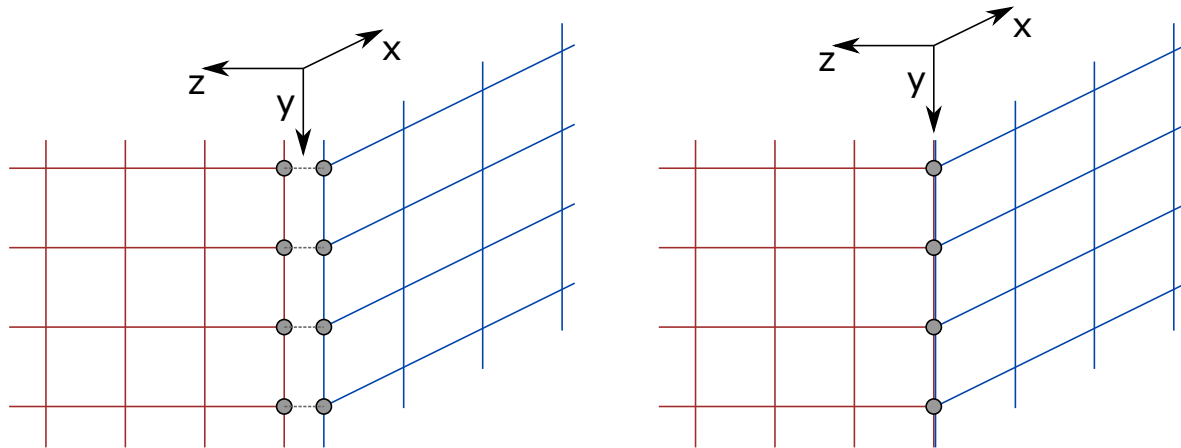


Figure 2. Example of how two adjacent parts are joined together with a weld element. The **left** panel shows the correspondence of nodes between both parts, however, the gap that appears is only introduced for the sake of clarity. On the **right** the actual position of both parts is shown, where corresponding nodes of each part are located exactly in the same place. The local reference system is also shown.

2.3. Spatial Discretization

The nonlinear problem described above is solved numerically and implemented using the commercial code LS-DYNA, a well suited program for strongly nonlinear materials and large deformations. The program implements the Finite Element Method to solve the problem.

In this case, since the attenuator is composed of metal sheets with a relative low thickness, we have decided to use three-dimensional quadrilateral shell elements with four nodes. Elements are fully integrated and five layers are used across thickness to increase the accuracy of the integration process.

2.4. Temporal Discretization

The problem studied in this paper is a transient problem, therefore it is needed to perform also a temporal discretization. Impact problems are relatively fast studies with strong non-linearities and large deformations. As a consequence, an explicit integration scheme is the most suitable method to solve them.

LS-DYNA uses explicit dynamic schemes to perform time integration of the solids mechanics equations (in particular, the central difference method is employed). The main drawback of these explicit methods is that they are potentially unstable, therefore the time step is computed in each cycle using the Courant-Friedrichs-Levy (CFL) criterion [34]. In addition, a safety factor of 0.9 is applied over the time step computed using the CFL criterion in order to ensure the stability of the method.

For each time step, the computation begins with the deformation of the nodes (data provided by the previous step or the initial conditions), producing a strain in the elements, and therefore, a stress-state that depends on the material's constitutive law. As a consequence, internal forces applied over the nodes can be computed and, in addition, external forces from boundary conditions, contacts and volumetric forces must be taken into account to calculate the total nodal forces. Finally, acceleration is obtained by dividing each nodal force by the corresponding nodal mass and, using the explicit integration scheme, velocity and displacement are computed. This procedure is then repeated for each time step until the final time is achieved.

3. Validation Case: Comparison with an Experimental Test

This model is constructed to reproduce an experimental test that was performed with the real attenuator. The details of the simulation model and experimental test are given below.

A general overview of the methodology is shown in Figure 3, left panel. As can be seen there, from the CAD geometry we define both mesh and boundary conditions of the finite element model. Then, the numerical resolution of the resulting nonlinear discrete problem is implemented using LS-DYNA package by using an iterative scheme. Once the convergence is achieved, a comparison with the experimental data is performed. On the contrary, the mesh is refined and the procedure starts again.

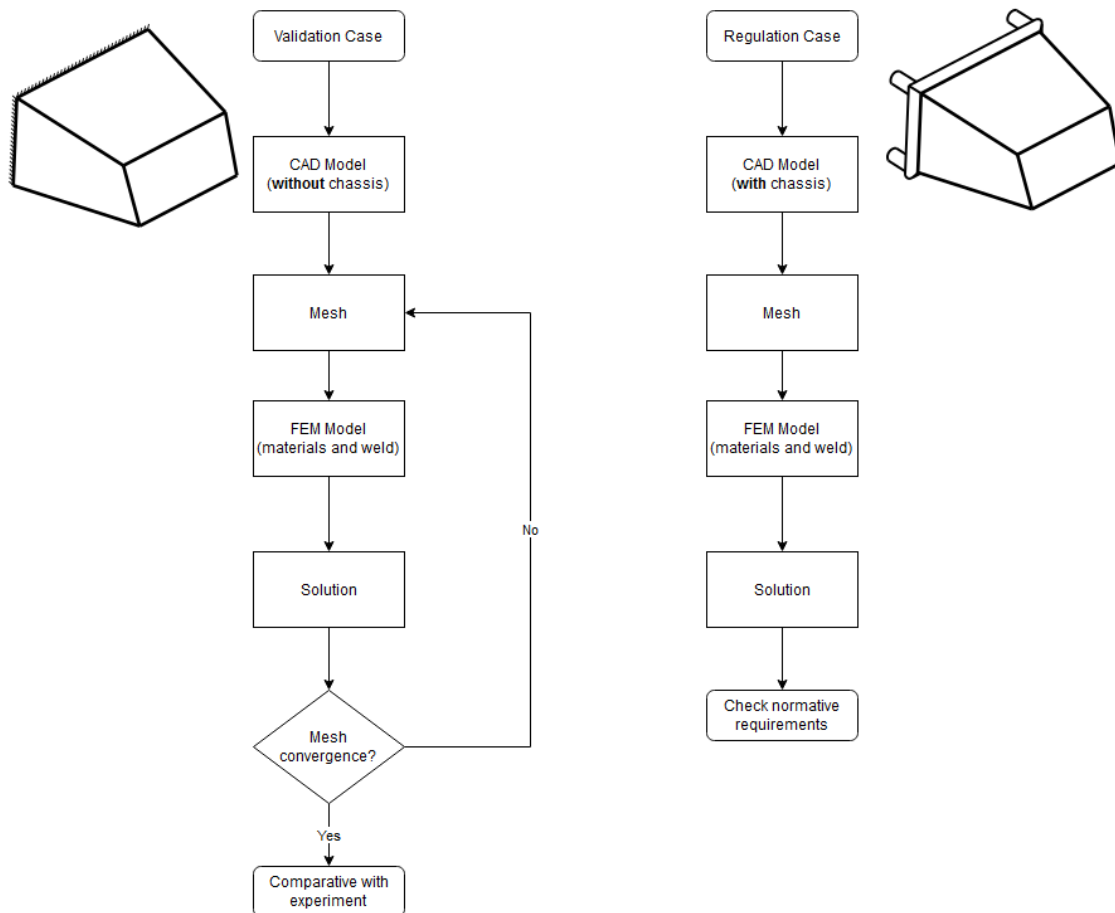


Figure 3. Flow chart of the numerical resolution.

The geometry of the attenuator consists of a truncated pyramid with rectangular base. The top of the pyramid is not flat but in a slight angle, and their dimensions are specified in Figure 1. Complying with the SAE-Formula regulations, the dimensions of the attenuator are within an envelope of $270.3 \times 159.8 \times 234.5 \text{ mm}^3$; the angles are also restricted. A three-dimensional view is also shown in Figure 4. The material for this part is a sheet of aluminum alloy (EN AW 5083-O) with a thickness of 2.5 mm (see Table 1 for details). As stated in the previous section, its plastic behavior is considered.

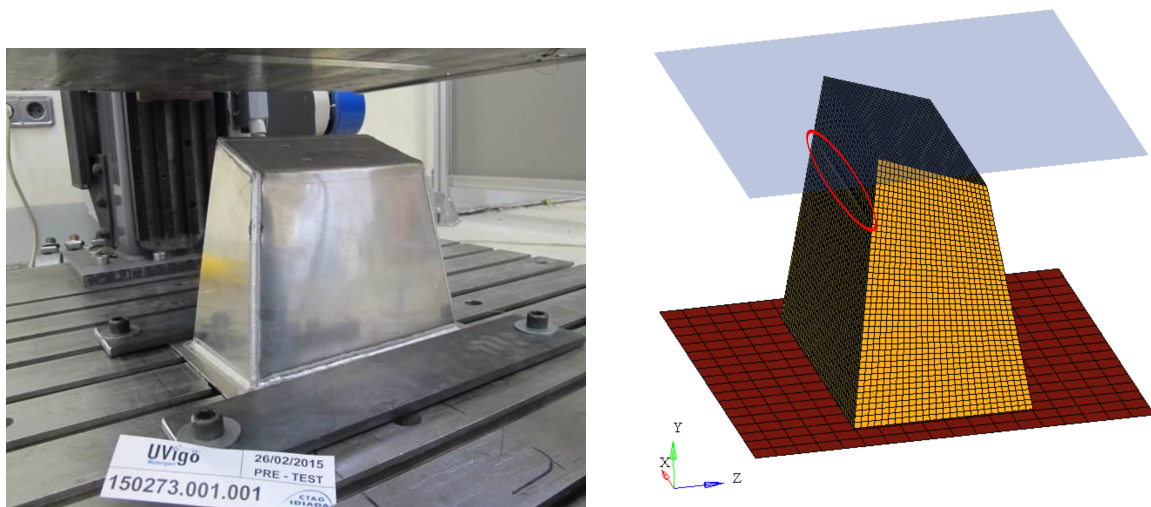


Figure 4. Experimental setup for the test and the mesh of the model.

Table 1. Mechanical properties of the aluminum used in our analysis. The values were taken after a general survey on reference providers.

Mechanical Properties	Values
Density (kg/m^3)	2700
Elastic Modulus (GPa)	72
Yielding Strength (MPa)	115
Poisson's ratio	0.33
Tangent Modulus (GPa)	1.082

The lateral walls are all welded together. The properties for this weld are the fillet width, which is set to 3 mm, and the fillet length computed as the length of the edge divided by the number of elements in that edge (it varies from 5.3 to 4.5 mm). The thickness for the weld is the same as for the plate. Finally, the strength of the union is considered 260 MPa, according to [35].

3.1. Real Test

The attenuator was tested in a drop tower, allowing a direct comparison with the computed results. The test was performed at CTAG-IDIADA Safety Technology in Spain. As specified in the applicable regulation, a block with a weight of 348 kg was dropped from 2.13 m into the attenuator (reaching a velocity of 6.47 m/s before the impact). To obtain the measurements, a high speed camera (1000 FPS) recorded the test, and an accelerometer (Kyowa Electronic Instruments) was installed on the impact block. The raw data from the accelerometer was analyzed with a Channel Filter Class CFC-60 (100 Hz) following the regulation SAE-J211 (see the raw data in Section 3.3). The attenuator was fixed to the floor on its base and the impact block advanced in the vertical direction. An image of the experimental setup is shown in Figure 4 (left panel).

3.2. Finite Element Model

To reproduce the test conditions, the attenuator in the model is fixed on its base. The impact block is modeled as a rigid body that advances to the attenuator and becomes in contact at the impact velocity. It is depicted in Figure 4, on the right panel, as a translucent blue surface. The welded and bonded walls are indicated in Figure 5, as well as a detail of the mesh in a welded edge. To study the influence of the welding two cases are simulated. The formulation for weld failure was defined in the previous section.

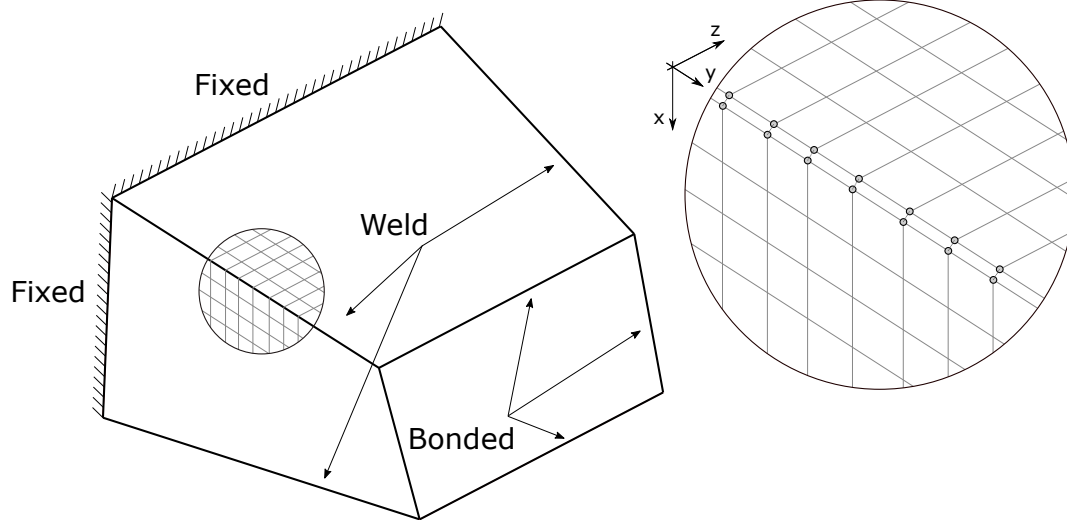


Figure 5. Boundary conditions and detail of the welding.

Regarding the mesh shown in Figure 4 (right panel), all the elements are defined as shells, and the discretization is made with quadrilateral elements (*quad 4*). We study several mesh sizes, in order to observe its convergence. This analysis is detailed in the results section. Bonded elements with nonconforming meshes are imposed as Multi-Point Constraint (MPC) boundary conditions with restricted rotations [36]. The contact with the impact block as well as the self-contact among the walls are modeled using a penalty formulation (see [37]).

To be able to reproduce the folding pattern in the real test, an initial small deformation is introduced (highlighted in Figure 4, right panel). This small defect (a deviation of the mesh nodes to the inside of the part) is located at 3/4 of the height and follows a cosine shape with one peak that will allow to reproduce the initial fold in the buckling pattern [29,38].

3.3. Results

The results of the simulations for the coarse and fine meshes are compared with the images and data from the experimental test. In Figure 6, it can be seen that, qualitatively, the simulation with the reference mesh (right panel) reproduces accurately the overall behavior of the part. In the top images, at time 37 ms, the weld is starting to fail in the simulation, and in the real test, the corresponding edge is subjected to a big deformation, also in the verge of failing. In the middle images, the failure has developed and the opening is clearly seen for both the test case and the simulation with the reference mesh. The weld fails in the same spot as in the experimental test and, thanks to the trigger, the failure of the weld resembles the opening that appears in the experiment. We note that for the coarse mesh (left panels) there is no weld failure. The simulation lasts 60 ms, the time it takes for the impact block to fully stop and the results are recorded in steps of 0.5 ms. These computations are performed with 64 Gb of RAM and an Intel-Core i7-4820K processor, the mesh sizes and computing times are described in Table 2.

Table 2. Mesh sizes and computing times.

Mesh	Nodes	Elements	Time
Ref. $\times 0.5$	3017	2732	6 min
Reference	8919	8440	27 min
Ref. $\times 1.5$	20,439	19,194	91 min

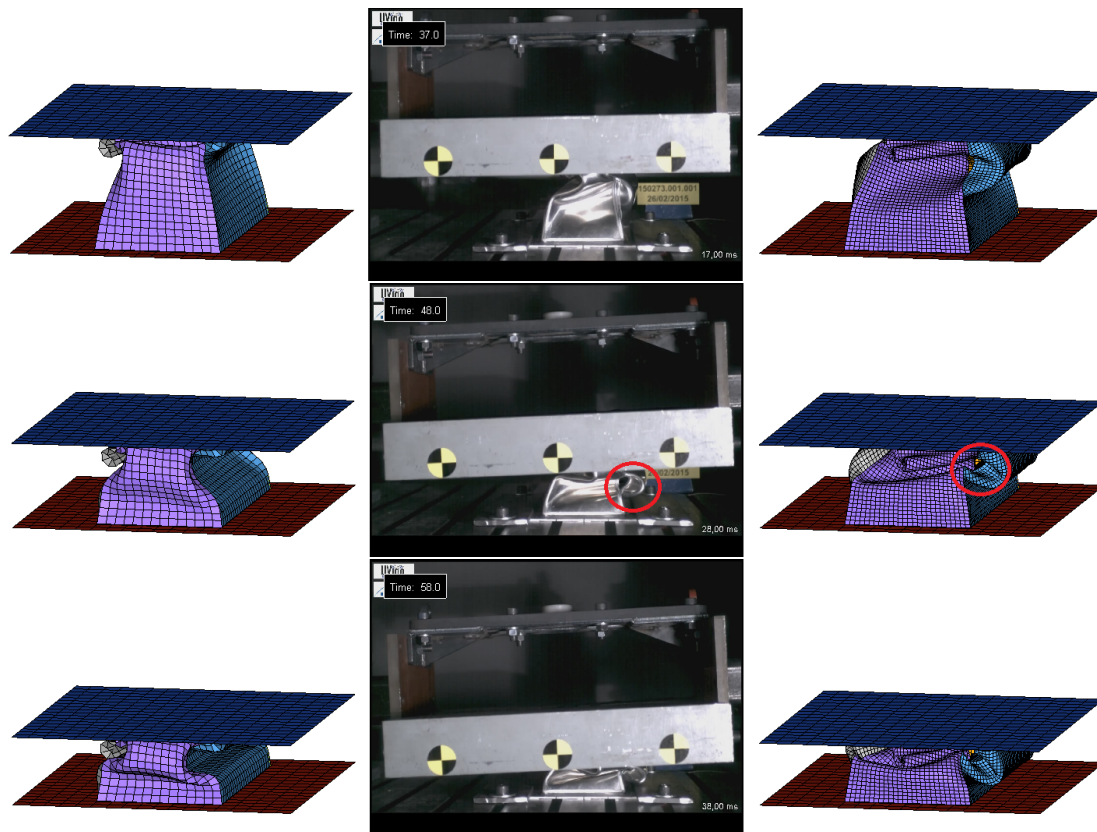


Figure 6. Images of the real test (center), and two simulations with a coarse (left) and fine (right) mesh. The snapshots were taken at at 37, 48 and 58 ms (from top to bottom). The opening of the welding is highlighted both in the real test and the model.

Regarding the deceleration of the impact block, the results for this magnitude, as the block descends, are represented in Figure 7. The unfiltered accelerometer data is shown in light gray, and the filtered values (processed with a CFC 100 Hz filter) in black. The numerical results are also filtered similarly to the experimental results. In the graph, a tendency to reproduce the test curve can be seen; however, it is difficult to obtain close quantitative results in explicit simulations where the time interval of interest lasts only a few milliseconds [39–41]. Also, the noise in the experimental data impedes quantitative comparisons. Regarding the convergence of the mesh, we show the results for the different mesh sizes, observing a convergence for the two smaller ones. Thus, since the results are similar and the computing time is significantly higher for the refined mesh, we only consider the reference mesh for further analysis. The different values for the green line (coarse mesh) are probably caused by a different folding pattern that generates self-contacts in the structure, as well as the absence of welding failure that can be seen in Figure 6 (left panels).

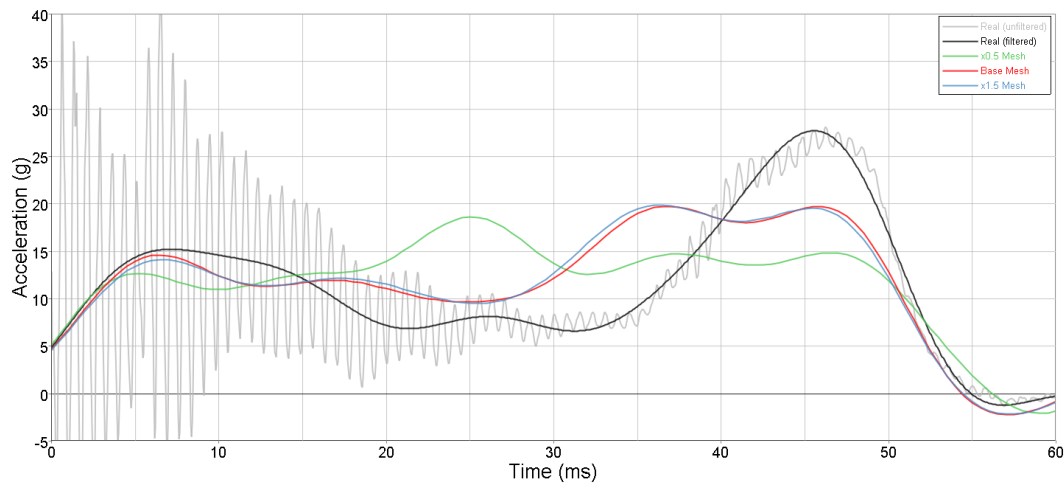


Figure 7. Acceleration of the impact block in the real test unfiltered (grey) and after filtering (black). The simulation cases for different meshes are represented in green (coarse mesh), red (the reference mesh) and blue (the finer mesh). We can see that the reference mesh is converged (minimal differences appear when the mesh is refined further).

4. Simulation of the Regulation Case

To validate the attenuator to be used in SAE-Formula a more complex set up is required. The front part of the chassis must be included in the analysis. This part consists of thin wall tubes that are attached to the bottom of the attenuator. Although the tubes at the bottom of the attenuator are not exactly the chassis ones, the regulation only requires a representative part of a chassis.

As in the previous section, a general overview of the methodology is shown in Figure 3, right panel. The flow chart is rather similar. The main difference is that, since we must not to compare the numerical results with real data, the solution is obtained directly. Then, we check the normative requirements.

Once we were able to reproduce the real test with the model, the complete model with the front part of the chassis is simulated. The absorber is now considered bonded to the tubes of the chassis and the part of the tubes of the chassis considered as fixed. The walls of the absorber are considered as welded with the possibility of failure (similarly to the previous example). The mesh employed for this example (with a mesh size equal to the reference mesh presented before) as well as the boundary conditions are shown in Figure 8.

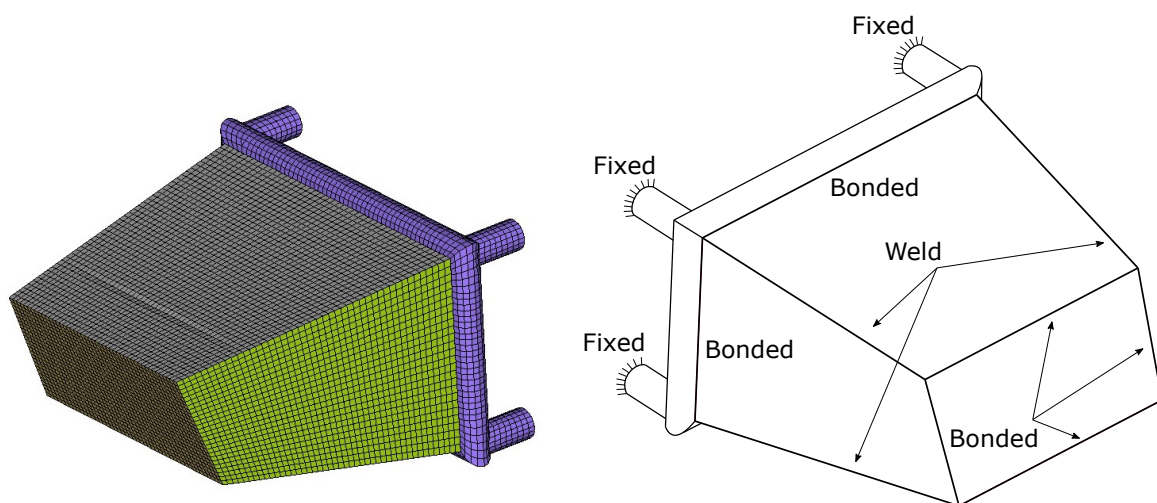


Figure 8. Mesh of the model with the front part of the chassis (left) and boundary conditions (right).

Results

In this section we aim to see if the part complies with the restrictions established in the regulation for this test. In Figure 9 some frames of the simulation are shown. It can be seen that, in this case, there is no failure in the welded parts (although it is implemented in the model), probably due to the energy absorption on the chassis tubes. If these results are compared with the ones from Figure 6 (right panels) it can be seen that the folding pattern is qualitatively the same.

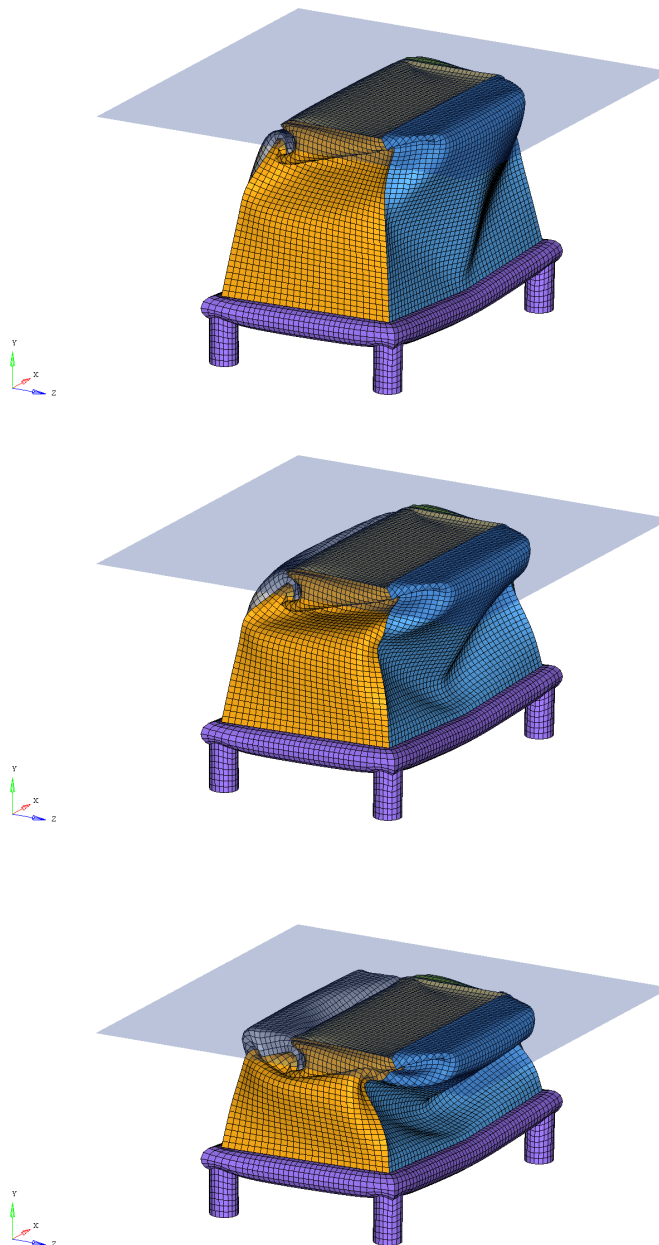


Figure 9. Images from the simulation of the test following the regulation conditions at 17, 22 and 38 ms.

Regarding the magnitudes that are established in the regulation, the first one studied is the acceleration of the impact block. In Figure 10 the acceleration of the block obtained with the simulation, and filtered as in the previous cases, is shown. The regulation restricts both the average and peak acceleration values to 20 g and 40 g, respectively. It is clear from the figure that both values are well below the requirements, with an average deceleration of around 15 g and a peak acceleration below 25 g.

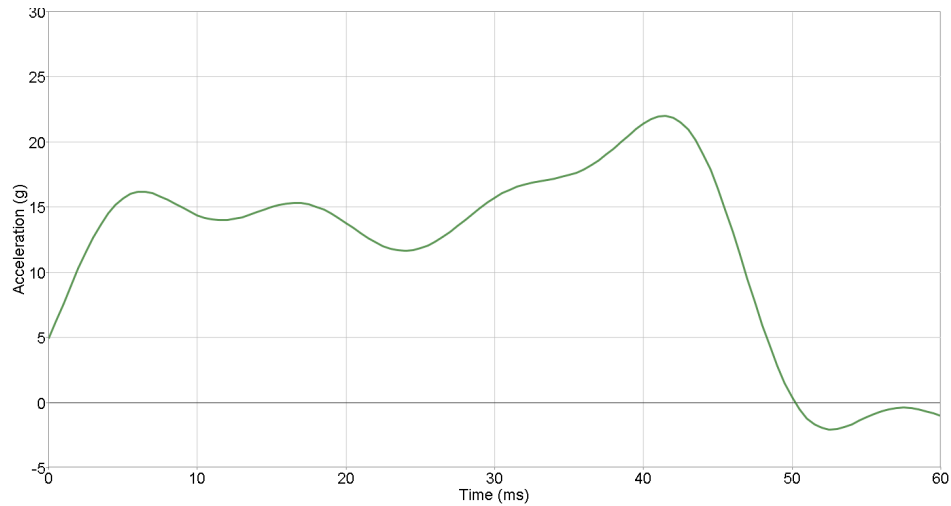


Figure 10. Acceleration of the impact block filtered with a CFC 100 Hz filter for the model with the front part of the chassis.

The other restricted magnitude is the maximum deformation of the front part of the chassis, allowing a maximum permanent displacement 25 mm. In Figure 11, the maximum displacement at any point of this part of the assembly is represented at time $t = 43$ ms. It can be seen that the maximum value obtained is well below the regulation standard and no relevant deformations appear in this front part of the chassis.

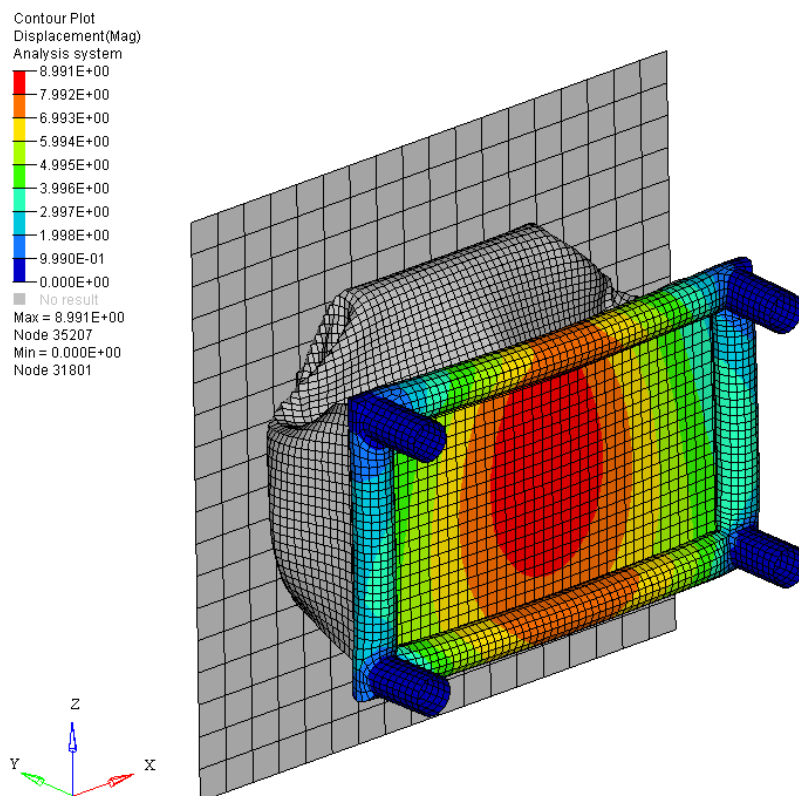


Figure 11. Displacement of the front part of the chassis (the base of the attenuator) at $t = 43$ ms (when the maximum deformation appears). The maximum displacement is 8.9 mm.

5. Conclusions

In this work, we analyzed, from the numerical point of view, the design of an impact attenuator for a Formula Student car. It led to a highly nonlinear problem due to the material behavior (elastoplasticity with isotropic hardening), the large deformations and also the welding behavior. A finite element model was presented and implemented using the commercial code LS-DYNA, and the results of a real test were reproduced both quantitatively and qualitatively. A sensitivity analysis was also performed to avoid the mesh dependency. The novelty of the work relied on the addition of a weld model for the walls and top unions of the attenuator, which allowed to reproduce the failure of a connection between two of the walls. The same finite element model was also used for the validation of a more complete model with the front part of the chassis. Results showed that the designed parts fulfilled the standard rules for the design of a Formula Student car.

Author Contributions: Conceptualization and Methodology J.B., J.A.L.-C. and S.S.; Software, Formal Analysis and Data Curation J.B., J.A.L.-C. and S.S.; Validation J.B. and A.S.; Supervision E.C., A.S. and J.R.F.; Writing Original Draft Preparation J.B., E.C. and J.R.F.; Writing Review and Editing E.C. and A.S.; Funding Acquisition A.S. and J.R.F. All authors have read and agreed to the published version of the manuscript.

Funding: This work has been partially funded by the research project PGC2018-096696-B-I00 (Ministerio de Ciencia, Innovación y Universidades, Spain) and the grant ED431C 2019/21 (Xunta de Galicia, Grupos de Referencia Competitiva). J. Baldonado acknowledges the funding by Xunta de Galicia (Spain) under the program Axudas á etapa predoutoral with Ref. ED481A-2019/230.

Conflicts of Interest: The authors declare no conflict of interest. The funders had no role in the design of the study; in the collection, analyses, or interpretation of data; in the writing of the manuscript, or in the decision to publish the results.

References

1. 2018 Formula SAE Rules; SAE International: Warrendale, PA, USA, 2018. Available online: <https://www.fsaeonline.com> (accessed on 10 March 2018).
2. Rooppakhun, S.; Boonporm, P.; Puangcha-um, W. Design and Analysis of Impact Attenuator for Student Formula. *SAE Tech. Pap.* **2015**. [[CrossRef](#)]
3. Mihradi, S.; Golfianto, H.; Mahyuddi, A.I.; Dirgantara, T. Head Injury Analysis of Vehicle Occupant in Frontal Crash Simulation: Case Study of ITB Formula SAE Race Car. *J. Eng. Technol. Sci.* **2017**, *49*, 534–545. [[CrossRef](#)]
4. Boria, S. Behaviour of an Impact Attenuator for Formula SAE Car under Dynamic Loading. *Int. J. Veh. Struct. Syst.* **2010**, *2*, 45–53. [[CrossRef](#)]
5. Jianhua, W.; Dashuai, X.; Shuai, Z.; Shichao, W. Designing and Experiment study on Front Impact Attenuator for Formula SAE Racecar. *Appl. Mech. Mater.* **2012**, *138–139*, 33–37.
6. Belingardi, G.; Boria, S.; Obradovic, J. Energy Absorbing Sacrificial Structures Made of Composite Materials for Vehicle Crash Design. In *Dynamic Failure of Composite and Sandwich Structures*; Abrate, S., Castanié, B., Rajapakse, Y., Eds.; Solid Mechanics and Its Applications; Springer: Berlin, Germany, 2013; Volume 192, pp. 577–609.
7. Yang, Y.; Wu, X.; Terada, S.; Okano, M.; Nakai, A.; Hamada, H. Application of FRP in a vehicle for Student Formula SAE Competition of Japan. *Int. J. Crashworth.* **2012**, *17*, 295–307. [[CrossRef](#)]
8. Segade, A.; López-Campos, J.A.; Fernández, J.R.; Casarejos, E.; Vilán, J.A. Finite Element Simulation for Analysing the Design and Testing of an Energy Absorption System. *Materials* **2016**, *9*, 660. [[CrossRef](#)]
9. Belingardi, G.; Obradovic, J. Design of the impact attenuator for a formula student racing car: Numerical simulation of the impact crash test. *J. Serbian Soc. Comput.* **2010**, *4*, 52–65.
10. Farlian, R.S.; Ubaidillah Krishna, E.K.; Muhamad, I.F.; Sukmaji, I.C.; Muhamad, H.I. Numerical simulation of several impact attenuator design for a formula student car. *AIP Conf. Proc.* **2018**, *1931*, 030036.
11. Chen, W.; Deng, X. Performance of shell elements in modeling spot-welded joints. *Finite Elem. Anal. Des.* **2000**, *35*, 41–57. [[CrossRef](#)]
12. Combescure, A.; Delcroix, F.; Caplain, L.; Espanol, S.; Eliot, P. A finite element to simulate the failure of weld points on impact. *Int. J. Impact Eng.* **2003**, *28*, 783–802. [[CrossRef](#)]

13. Langrand, B.; Combescure, A. Non-linear and failure behaviour of spotwelds: a global finite element and experiments in pure and mixed modes I/II. *Int. J. Solids Struct.* **2004**, *41*, 6631–6646. [[CrossRef](#)]
14. Matzenmiller, A.; Schweizerhof, K.; Rust, W. Joint failure modeling in crashworthiness analysis. In Proceedings of the Second International LS-DYNA3D Conference, San Francisco, CA, USA, 20–21 September 1994.
15. Xiang, Y.; Wang, Q.; Fanb, Z.; Fang, H. Optimal crashworthiness design of a spot-welded thin-walled hat section. *Finite Elem. Anal. Des.* **2006**, *42*, 846–855. [[CrossRef](#)]
16. Xu, S.; Deng, X. An evaluation of simplified Finite element models for spot-welded joints. *Finite Elem. Anal. Des.* **2004**, *40*, 1175–1194. [[CrossRef](#)]
17. Zhang, Y.; Taylor, D. Optimization of spot-welded structures. *Finite Elem. Anal. Des.* **2001**, *37*, 1013–1022. [[CrossRef](#)]
18. Langrand, B.; Markiewicz, E. Strain-rate dependence in spot welds: Non-linear behaviour and failure in pure and combined modes I/II. *Int. J. Impact Eng.* **2010**, *37*, 792–805. [[CrossRef](#)]
19. Schneider, F.; Jones, N. Influence of spot-weld failure on crushing of thin-walled structural sections. *Int. J. Mech. Sci.* **2003**, *45*, 2061–2081. [[CrossRef](#)]
20. Choi, Y.; Kim, J.; Park, Y.W.; Rhee, S. Development of a Spot Weld Analysis Model That Incorporates Strain Rate. *Int. Precis. Eng. Manuf.* **2012**, *13*, 245–251. [[CrossRef](#)]
21. Blatnický, M.; Sága, M.; Dižo, J.; Bruna, M. Application of Light Metal Alloy EN AW 6063 to Vehicle Frame Construction with an Innovated Steering Mechanism. *Materials* **2020**, *13*, 817. [[CrossRef](#)]
22. Marques, E.S.V.; Silva, F.J.G.; Pereira, A.B. Comparison of Finite Element Methods in Fusion Welding Processes—A Review. *Metals* **2020**, *10*, 75. [[CrossRef](#)]
23. Chang, P.H.; Teng, T.L. Numerical and experimental investigations on the residual stresses of the butt-welded joints. *Comput. Mater. Sci.* **2004**, *29*, 511–522. [[CrossRef](#)]
24. Anca, A.; Cardona, A.; Risso, J.; Fachinotti, V.D. Finite element modeling of welding processes. *Appl. Math. Model.* **2011**, *35*, 688–707. [[CrossRef](#)]
25. Deng, D.; Murakawa, H.; Liang, W. Numerical simulation of welding distortion in large structures. *Comput. Methods Appl. Mech. Eng.* **2007**, *196*, 4613–4627. [[CrossRef](#)]
26. Wang, R.; Zhang, J.; Serizawa, H.; Murakawa, H. Study of welding inherent deformations in thin plates based on finite element analysis using interactive substructure method. *Mater. Des.* **2009**, *30*, 3474–3481. [[CrossRef](#)]
27. Bucolo, M.; Buscarino, A.; Famoso, C.; Fortuna, L.; Frasca, M. Control of imperfect dynamical systems. *Nonlinear Dyn.* **2019**, *98*, 2989–2999. [[CrossRef](#)]
28. López-Campos, J.A.; Segade, A.; Casarejos, E.; Fernández, J.R.; Vilán, J.A. A finite element model to study weld and geometric imperfections in an impact attenuator device. In Proceedings of the IRF2018: 6th International Conference Integrity-Reliability-Failure, Lisbon, Portugal, 22–26 July 2018.
29. Langseth, M.; Hopperstad, O.S.; Berstad, T. Crashworthiness of aluminium extrusions: validation of numerical simulation, effect of mass ratio and impact velocity. *Int. J. Impact Eng.* **1999**, *22*, 829–854. [[CrossRef](#)]
30. Hirose, S. Shock Absorbing Member. Patent PCT No. PCT/JP2012/070109, 7 February 2014.
31. Yuen, S.C.K.; Nurick, G.N. The energy-absorbing characteristics of tubular structures with geometric and material modifications: an overview. *Appl. Mech. Rev. Trans. ASME* **2008**, *61*, 1–15. [[CrossRef](#)]
32. Stout, M.G.; Rollett, A.D. Large-strain Bauschinger effects in fcc metals and alloys. *Metall. Trans. A* **1990**, *21*, 3201–3213. [[CrossRef](#)]
33. Zienkiewicz, O.C.; Taylor, R.L. *The Finite Element Method*; Butterworth-Heinemann: Oxford, UK, 2000; Volume 2.
34. Mullen, R.; Belytschko, T. An analysis of an unconditionally stable explicit method. *Comput. Struct.* **1983**, *16*, 691–696. [[CrossRef](#)]
35. Mutombo, M. Mechanical properties of 5083 aluminium welds after manual and automatic pulsed gas metal arc welding using E5356 filler. *Mater. Sci. Forum* **2010**, *654–656*, 2560–2563. [[CrossRef](#)]
36. Abel, J.F.; Shephard, M.S. An algorithm for multipoint constraints in finite element analysis. *Int. J. Numer. Methods Eng.* **1979**, *14*, 464–467. [[CrossRef](#)]
37. Huněk, I. On a penalty formulation for contact-impact problems. *Comput. Struct.* **1993**, *48*, 193–203. [[CrossRef](#)]

38. Zarei, H.R.; Kroger, M. Multiobjective crashworthiness optimization of circular aluminum tubes. *Thin-Walled Struct.* **2006**, *44*, 301–308. [[CrossRef](#)]
39. Borvik, T.; Hopperstad, O.S.; Reyes, A.; Langseth, M.; Solomos, G.; Dyngel, T. Empty and foam-filled circular aluminium tubes subjected to axial and oblique quasistatic loading. *Int. J. Crashworth.* **2003**, *8*, 481–494. [[CrossRef](#)]
40. Langseth, M.; Hopperstad, O.S.; Hanssen, A.G. Crash behaviour of thin-walled aluminium members *Thin-Walled Struct.* **1998**, *32*, 127–150. [[CrossRef](#)]
41. Yan, W.; Durif, E.; Yamada, Y.; Wen, C. Crushing simulation of foam-filled aluminium tubes. *Mater. Trans.* **2007**, *48*, 1901–1906. [[CrossRef](#)]



© 2020 by the authors. Licensee MDPI, Basel, Switzerland. This article is an open access article distributed under the terms and conditions of the Creative Commons Attribution (CC BY) license (<http://creativecommons.org/licenses/by/4.0/>).